Ytterbium fiber laser welding of Ti6Al4V alloy

Ytterbium fiber laser welding of Ti6Al4V alloy

Giuseppe Casalino[1], Michelangelo Mortello[1, *], Sabina L. Campanelli[1]

[1]Politecnico di Bari, Dipartimento di Meccanica Matematica e Management (DMMM). Viale Japigia 182, Bari 70126, Italy.

*Corresponding author: Michelangelo Mortello

Telephone: +390805962753

E-mail address: Michelangelo.mortello@poliba.it.

Abstract

In this work, full penetration welding of 2 mm thick Ti6Al4V plates in butt configuration was performed by adopting a high brightness Yb fiber laser. Neither groove preparation nor filler groove was used. The influence of different welding conditions on the bead morphology, metallurgy and mechanical properties was discussed in details. Seam appearance and microstructures were assessed by optical microscopy, while the mechanical behavior was evaluated in terms of Vickers micro-hardness and tensile strength. Fracture surfaces were inspected by scanning electron microscopy. The efficiency of the welding process was estimated by correlating the power transmitted and the extension of the fusion zone. A low degree defectiveness was reached by optimizing the welding conditions.

Key-words: fiber laser welding, Ti6Al4V titanium alloy, metallurgical and mechanical properties.

1. Introduction

In the last years, the demand for lightweight materials has increased considerably, mostly in industries for which fuel consumption and resistance to severe working conditions are critical aspects. In particular, the use of titanium alloys is spreading rapidly in numerous fields. Thanks to their high strength-to-weight ratio, fracture toughness, corrosion resistance, good fatigue behavior and desirable high temperature properties, these alloys are currently employed for many aerospace, nuclear and automotive applications [1-3]. Moreover, the high bio-compatibility has extended the use of titanium alloys to the production of bio-medical devices [4]. α-β two-phase alloys are currently the most common among all Ti alloys, thanks to the possibility to vary the mechanical and physical properties

by either modifying the percentage of the alloying elements or controlling the microstructural evolution during thermo-mechanical processing.

Many joining techniques have been developed to perform Ti assemblies, including solid state and fusion welding [5-10]. Laser welding is one of the most suitable joining technique performing metal assemblies [11]. A wide range of intricate weld geometries and configurations can be produced with high levels of productivity, quality and flexibility. Narrow bead width, high precision and low panel distortions are guaranteed by the high energy density in small spot dimensions. Among commercially available lasers, the fiber source presents low capital investment requirements and several remarkable technical advantages, which can potentially improve the quality of the seam. When it comes to the fiber laser, the good beam quality coupled with high CW powers offers deep penetration welding as well shallow conduction mode welding. These lasers can be used in a diversity of materials as the low wavelength allows absorption by almost all metals and alloys [14 bis]. As demonstrated by Caiazzo et al., an appreciable improvement in seam quality was also achieved by adopting disk laser source [14]. In spite of the above mentioned benefits, laser welding requires low gap tolerance and accurate alignment of the pieces. Moreover the successfully outcome of the process is strictly dependent on the keyhole behavior, whose stability derives from the complex balance between periodical recoil pressure and surface tension of the surrounding walls. If the keyhole collapses, the penetration depth is lower and gas bubbles are trapped in the weld pool, which lead to porosities.

The optimization of process parameters is a basic requirement for keyhole stability, as confirmed by previous works conducted in both pulsed and continuous wave (CW) regime. Schneider e al. achieved a significant improvement of process stability by optimizing the shielding gas flow rate for suppressing the vapor plume [15]. Akman et al. showed how to control penetration depth and bead geometry by controlling the laser output parameters [16]. Squillace et al. investigated the underfill defect formation and mechanical properties for different welding regimes and specific heat inputs [17]. Gao et al. showed how to decrease the porosity content by increasing the overlapping factor, which assists pores to escape from the melt pool [18]. Elements of statistical inference were assessed by Casalino et al., which interpolated experimental data by artificial neural network (ANN) with the aim to compute the significance of several parameters and their interactions on bead characteristics [19].

In this work Ytterbium CW fiber laser welding of 2 mm thick Ti6Al4V plates was investigated. A slight defocusing (2 mm under the top surface) was adopted. Process parameters were optimized by preliminary bead-on-plate tests. Depending on the fused zone appearance, two different seam morphologies were determined depending on the thermal input transmitted to the work-piece, i.e. V-

shaped and X-shaped ones. The joint quality was characterized in terms of weld morphology, microstructure and mechanical properties. The use of a fiber laser enhanced the quality of the weld for both bead appearance and mechanical behavior and a low level of defectiveness was reached.

2. Experimental

In this study, 2 mm thick plates were autogenously welded in butt configuration. The size of the sheets (length x width) was 100 x 50 mm. The material consisted of Ti6Al4V two-phase (α-β) titanium alloy in annealing condition. The chemical composition, mechanical properties and thermo-physical properties are listed in tables 1, 2 and 3, respectively.

Table 1 Chemical composition of the as-received material (weight %).

	Ti	Al	H	Mg	Fe	Mn	Si	Cr	O	Cu	N	C	V	W
Ti6Al4V	Balance	0.40	2.60	-	0.50	-	-	-	0.20	-	-	0.10	0.40	0.30

Table 2 Mechanical properties of the as-received material: ultimate tensile strength (UTS), yield stress (YS), Young module (E), elongation to fracture %(A %), Vickers microhardness (HV).

	UTS (MPa)	YS (MPa)	E (GPa)	A%	HV
Ti6Al4V	950	880	114	14	349

Table 3 Thermo-physical properties of the as received material: thermal conductivity (K), melting temperature (Tm), density (ρ).

	K (W/(m.K))	Tm (°C)	ρ (g/ cm ^{3})
Ti6Al4V	6.7	1650	4.43

Prior to welding the sheets were machined at low milling speed, wire brushed and cleaned with acetone. A high brightness fiber laser source was used in continuous wave regime. The active gain medium consisted in a 200 μm diameter optical fiber. Collimating lens and focusing lens with a focal length of 120 mm 250 mm respectively were used to deliver the beam to the workpiece. A slight defocusing (2 mm under the top surface) was adopted. Consequently, a focus spot of about 400 μm diameter (1/e^2 width) near-Gaussian distribution was produced on the surface. The sheets were fixed to the support by four clamps.

As suggested by Schneider et al. a suitable flow rate is useful to prevent the vapor plume [15]. However, as described by Katayama [21], since Ar has a higher density than both He and atmosphere air, it is convenient to introduce Ar and He at the upper and bottom surfaces, respectively. A flow rate of 15 l/min was used for both. A shielding gases equipment protected the crown and root of the molten pool from contamination by harmful atmospheric gases. The shielding device was made up of a metallic chamber, placed upon the pieces, into which polyethylene (PE) pipes converged the protecting gas. Figure 1 shows a picture of the protection system, while figure 2 contains the drawing of the shielding device, which introduce Ar gas upon the upper surface.

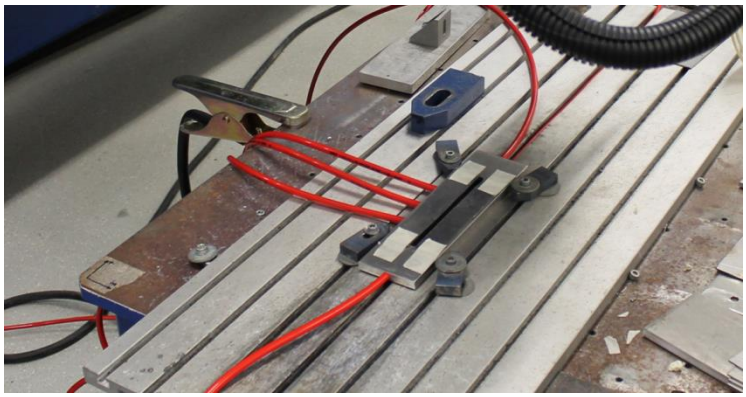

Fig.1 Shielding gases equipment

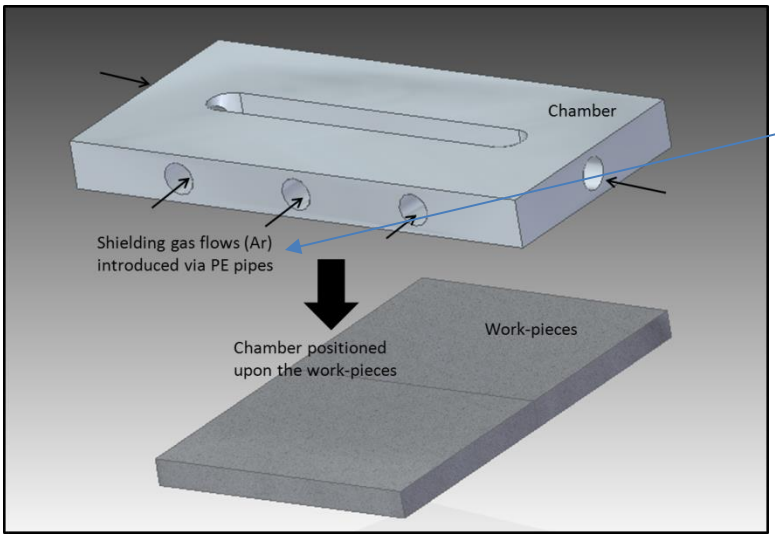

Sostituire

Inlet gas flow through PE pipes

NB cambiare l'immagine anche nel file delle figure

Fig.2 Shielding device function

Preliminary bead-on-plate tests were conducted to find suitable values of process parameters. Trials tests were performed for ensuring satisfactory penetration and avoiding lack of fusion zones. The power level was kept constant at 1.20 kW, whereas the welding speed ranged between 1000 and 2500

mm/min (see Table 4). The table also provides the linear energy (L.E.) adopted to perform the welds. It consists of the ratio of the power transmitted (P) to the welding speed (v), as indicated by the equation 1:

$$L.E. = \frac{P}{v} \quad \text{(eq. 1)}$$

Table 4 Process parameters adopted.

Sample	Laser power (kW)	Welding speed (m/min)	Linear energy (J/mm)
1	1.20	1.00	72.0
2	1.20	2.00	36.0
3	1.20	2.25	32.0
4	1.20	2.50	28.8

Various types of specimens were needed to provide a satisfactory evaluation of weld properties. Thus assemblies were visually inspected, cross-sectioned perpendicularly to the welding direction, polished with standard grinding procedures and chemically etched by Keller's reagents solution (1% HF, 1.5% HCl, 2.5% HNO_3 and 95% H_2O). This preparation procedure was aimed to study the most significant features in the weld zone. Microstructure was observed by optical microscopy (OM).

The efficiency of the welding process was evaluated by correlating the area of the fusion zone in the cross section with the transmission power [22]. Thus, a parameter called welding process efficiency (WPE) was introduced to take into account the amount of energy spent to generate a fusion zone in the work-piece. The definition of the WPE was expressed by the equation 2:

$$WPE = \frac{A_{FZ}}{L.E.} \quad \text{(eq. 2)}$$

where A_{FZ} is the area of the fusion zone, while L.E. is the linear energy (see eq. 1).

Two specimens with a 20 mm width and 100 mm length were cut from each joint and tensile tested perpendicularly to the welding line. The tests were conducted at room temperature by adopting a cross-head speed of 0.04 mm/min. The same procedure was adopted for two specimens taken from the parent metal. The average values of tensile strength and elongation % were compared to each other with the aim to determine the reduction in tensile properties occurred for each welding condition in comparison with the as-received material. Fracture surfaces were inspected through electron scanning microscopy (SEM).

Vickers micro-hardness tests were conducted at the mid thickness of the cross section through a pyramid indenter with a dwell time of 20 s and a test load of 200 g. The distance between two neighboring indentations was 0.25 mm. The spatial gradient of the micro-hardness (MHG), defined as the ratio of the hardness difference between the fusion zone (HV_{FZ}) and base metal (HV_{BM}) to the heat affected zone heat affected zone width ($WIDTH_{HV}$) (eq. 3), was calculated and discussed.

$$MHG = \frac{HV_{FZ} - HV_{BM}}{WIDTH_{HV}} \quad \text{(eq.3)}$$

3. Experimental results

3.1 Bead appearance

Since the power input was kept constant, the difference in welding speed was indicative of the different specific heat input. This last can be expressed in terms of linear energy (see equation 1). Therefore the main characteristics of samples 1 and 4, which were performed with a large difference in welding speed, were discussed to present two different seam morphologies and comprehend the corresponding thermodynamic behaviors. Figure 3 and 4 show the bead appearances of samples 1 and 4, respectively. Several discernible zones, resulting from different thermal cycles in the work-pieces, were indicated for both the macrographs. Full penetration condition was achieved. Thanks to the preparation procedure and process parameters, the main geometric defects, such as underfill, misalignment, sagging, undercut, lack or excessive penetration were within acceptable limits. Although overfill is generally produced because of the filler wire deposition, it can also occur during autogenous welding. It derives from the combination of various contributes that influence the motion of the weld pool. Excess of shielding gas flow, longitudinal metal liquid flow, contraction of plates and insufficient welding speed are the most influent factors [23].

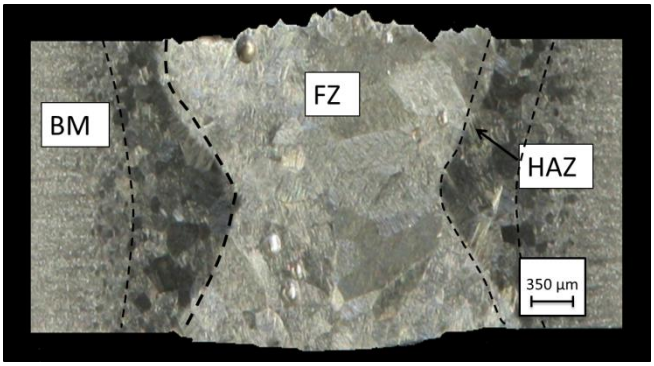

Fig.3 Cross section of sample 1 (P=1.20 kW, v=1.00 m/min).

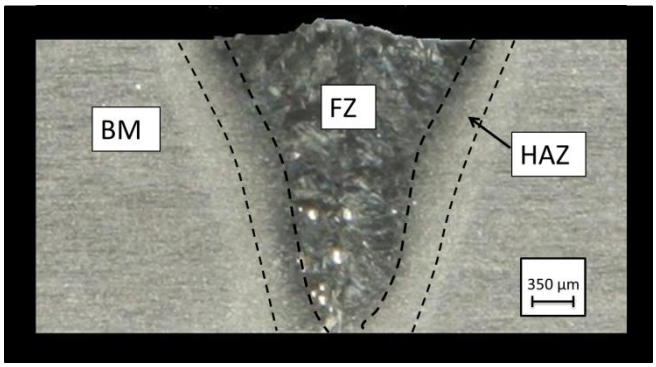

Fig.4 Cross section of sample 4 (P=1.20 kW, v=2.50 m/min).

Since the heat transfer in the weld pool mostly occurred by convection, the bead shape was determined by the fluid-dynamics of the weld pool. As demonstrated by Squillace et al. [17], the main aspects concern surface tension, vapor pressure, volume contraction, gravity and phase transformation. As explained by Lathabai et al. [6], the root bead increases with the thermal conductivity leading to the destabilization of the weld pool. The process stability in Ti alloys is less challenging than that in Al alloys.

Sample 1 presented an X-shaped bead, almost symmetric respect to the mid thickness. Zhang et al. [24] explained that the temperatures at the bottom surface are higher than those at the top surface. It follows that the bottom part of the weld pool was subjected to a lower surface tension. Moreover, during the source motion, the overheating of the root of the weld pool involved clockwise vortex, which favored the growth of the lower molten area. Since the welding speed value was rather low, the high linear energy caused the increase in time of the exposure of the liquid material to the laser irradiation. The prolonged direct irradiation brought the laser beam to pass through the keyhole, leading to energy loss.

On the other hand, sample 4 was performed with higher welding speed (lower linear energy). Since the heat input was lower in comparison with sample 1, the HAZ and FZ widths were smaller. When the laser energy irradiation was low the keyhole size did not increase. So, surface tension in the bottom part of the melt wall counterbalanced recoil forces and led to the formation of a V-shaped bead. Several macro-pores, whose diameter was in between few tens and 100 µm, were observed in both the upper part and the root of the FZ. They probably depend on both keyhole size and shape collapsing, which causes fluctuation during the process. In sample 4, pores localized in the lower zone of the bead. As the recoil pressure did not support the surface tension of the expanding molten walls, the keyhole collapsed leading to the entrapment of gas bubbles, which tried to escape upward in the weld pool. As concerns X-shaped bead, the keyhole collapsed and bridged keyhole walls at the middle region. The velocity at which the keyhole collapse was higher in the upper part than that in

the lower one of the weld pool. Consequently, as showed by figure 4, metallic vapors were trapped in the upper part of the bead.

Table 5 shows the values of LE, FZ area and WPE (see eq. 1 and 2) for samples 1 and 4, which were performed with the maximum and the minimum value of LE, respectively.

Table 5 Process parameters adopted.

Sample	LE (J/mm)	FZ area (mm^2)	WPE (mm^3/J)
1	72.0	3.4	0.047
4	28.8	1.8	0.062

Sample 4 (V-shaped bead) presented a higher WPE. This is probably due to the fact that during the welding of sample 1 (X-shaped bead) major overheating and internal heat conduction occurred. Thus, a greater amount of energy was lost in the material without being spent for increasing the area of the fusion zone. It follows that the percentage of energy converted in increase of weld zone was greater in the case of sample 4. Therefore, if one considers the efficiency of the process in these terms, the V-shaped condition appears to be favorable.

3.2 Microstructure

As indicated in figure 5, the microstructure of the as-received two-phaseTi6Al4V alloy consisted chiefly of intergranular body centered cubic β phases (dark colored) dispersed in a domain of equiaxed hexagonal close packed α phases (light colored).

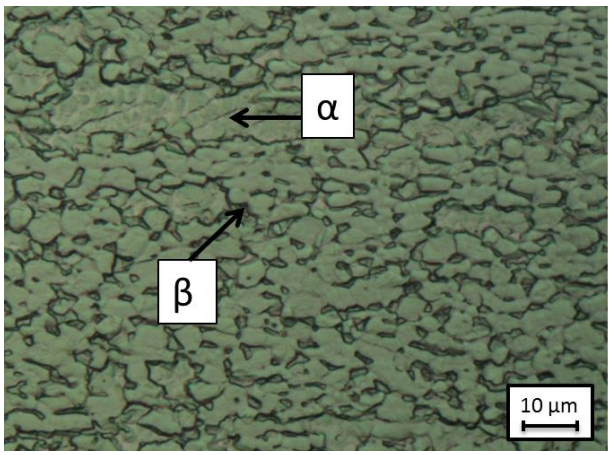

Fig.5 Microstructure of the as-received material.

The diameters of α and β grains were in the range of 5-15 μm and 1-5 μm, respectively. The process-related thermal cycles altered the crystallographic properties of the weld zone. The high temperature gradient and peak during the heating and cooling phases promoted a microstructure gradient. The reversible allotropic transformations during the heat treatment of Ti alloys are also influenced by the concentration of alloying elements and contaminants, which tend to stabilize one of the two phases. Figure 6 shows the microstructure in the FZ.

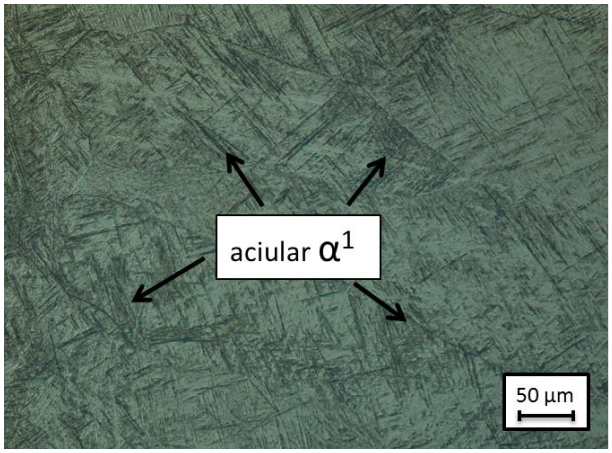

Fig. 6 Microstructure of the FZ of sample 4.

During the solidification phase, β grains grew along the direction of the heat flows. The rapid cooling rate in the weld pool, above the critical value for a full martensitic transformation, promoted the microstructural evolution from β to α^1 martensitic structure. The same effect can be obtained by quenching above the β transus temperature. Thus, a fully acicular α^1 solidification structure formed within prior coarse β grains. Figure 7 shows that the HAZ exhibits a more complex structure. Since the morphology of the seam, made up of primary α, blocky α, martensitic α^1 and β, was high heterogeneous in various zones, it was not simply to discriminate the different microstructures.

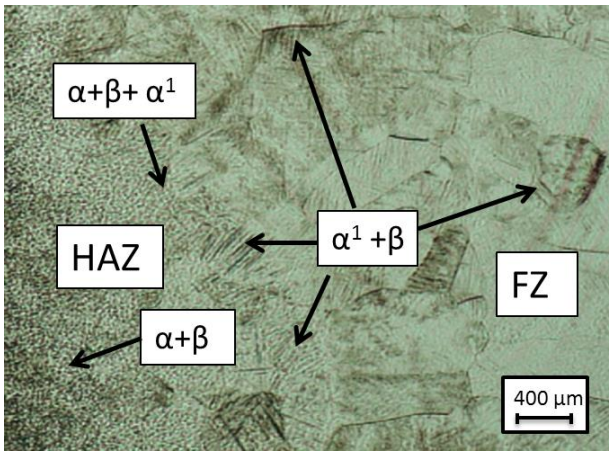

Fig. 7 Microstructure of the FZ/HAZ of sample 4.

Depending on the distance from the FZ, the HAZ was affected by different peak temperature and related cooling rate. Because of the temperature gradient, the microstructure in the HAZ evolved from a rich α^1 region (near the FZ) to a poor α1 region (far from the FZ). In fact, the regions close to the BM were subjected to a lower temperature. This gradient in microstructure presented the typical appearance of that achieved by quenching from a temperature below the β transus.

3.3 Micro-hardness

Figure 14 shows the micro-hardness profile at the mid thickness of the cross section of sample 4. Because of the microstructural modifications, which occurred during the process, a large gradient in micro-hardness was achieved. In particular, the hardness gradient value measured (see eq. 3) for sample 4 was about 110 HV/mm, since the HAZ width was about 0.7 mm, while the hardness in the BM and FZ were approximately equal to 340 and 420, respectively.

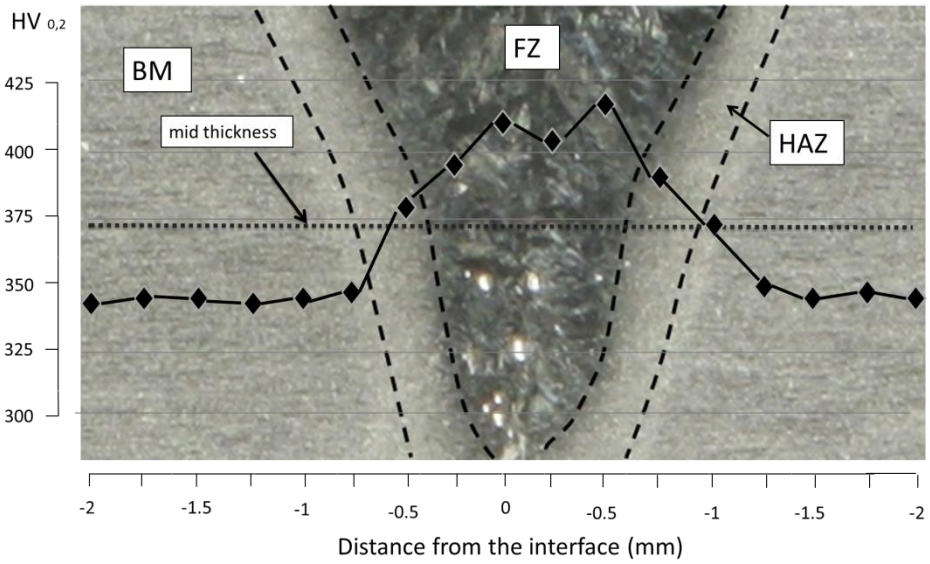

Fig. 14 Vickers micro-hardness profile at the mid thickness of cross section of sample 4.

The hardness trend detected in the BM was approximately constant with a mean value of about 340 HV. The profile appeared composed of scattered values, due to the inhomogeneous microstructure. The rapid cooling rate promoted the formation of acicular martensite structure, distributed with a certain gradient, in function of the thermal cycles and local material properties. Because of the full martensitic transformation, FZ exhibited peak values around 410 HV. The values reached in the HAZ sharply ranged from 350 HV (at the interface between the BM and the HAZ) to 390 HV (in proximity to the FZ). Moreover, as explained above, the imperfect protection of the weld pool did not prevent

completely the formation of brittle phases (mostly oxides and nitrides). As a consequence several zones were subjected to undesirable local embrittlement and hardening.

3.4 Tensile properties

The histograms in figures 8 and 9 summarize the mechanical behavior of both the welds and the parent metal. The mean values of tensile strength and elongation % for each welding condition are indicated. Black bars show the range between the maximum and minimum values for each sample.

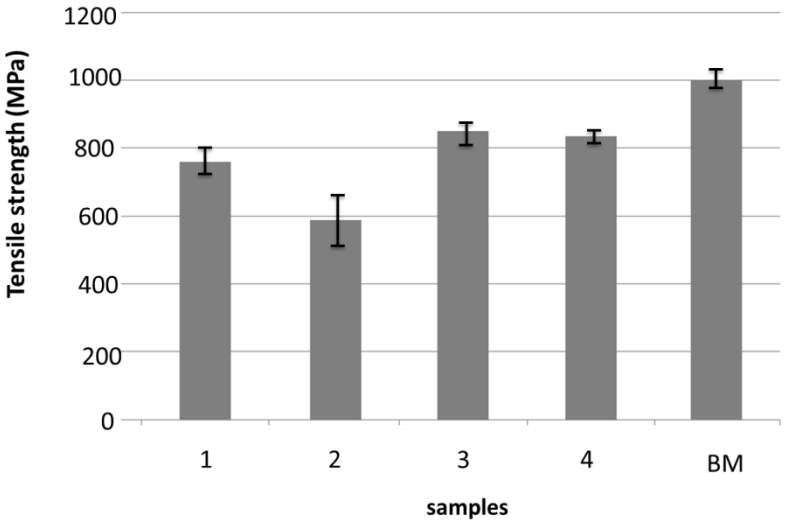

Fig. 8 Ultimate tensile strength.

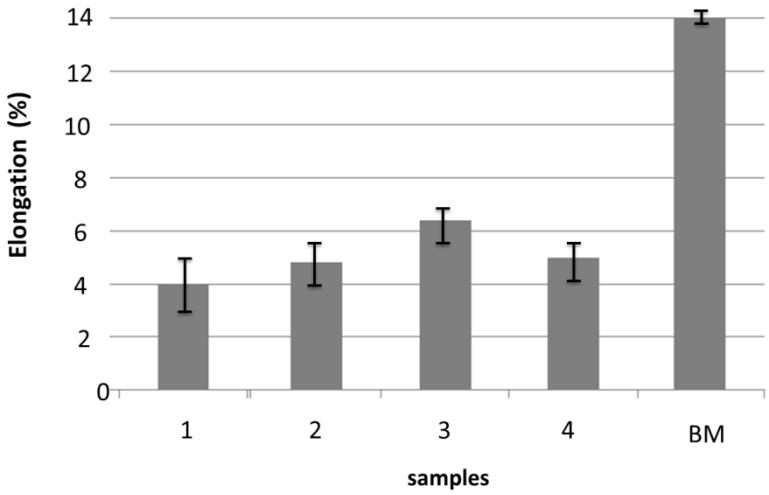

Fig. 9 Final elongation %.

Welded specimens exhibited a reduction in the ultimate tensile strength of about the 20% whereas the reduction in elongation ranged between the 60% and 70%. The mechanical resistance of sample

2 resulted to be significantly lower in comparison with other working conditions. The variability of mechanical properties in function of various combinations of process parameters was due to a variable degree of defectiveness. Unstable welding condition of the keyhole dynamics, favored porosity, contaminations, cracks and geometric defects, leading to a reduction in the mechanical properties.

Figure 10 shows the stress-strain curves for samples 1, 4 and parent metal one. Although, as mentioned above, two specimens for each welding conditions were tested, the diagram shows just one curve for each sample (it was chosen the specimen with the higher resistance for each welding condition).

Examining the stress-strain curve drives the following results. From the elastic field, it can be observed that the Young's modulus, yield strength and the resilience of the metal did not vary significantly.

Tensile strength and hardness rose at the expense of ductility and toughness. In fact, a significant loss in plasticity occurred. The significant growth of the grain size contributed to the tensile properties downgrading. Also scatter porosity in the weld pool promoted a reduction of the tensile properties. This involved a significant reduction of elongation % and toughness.

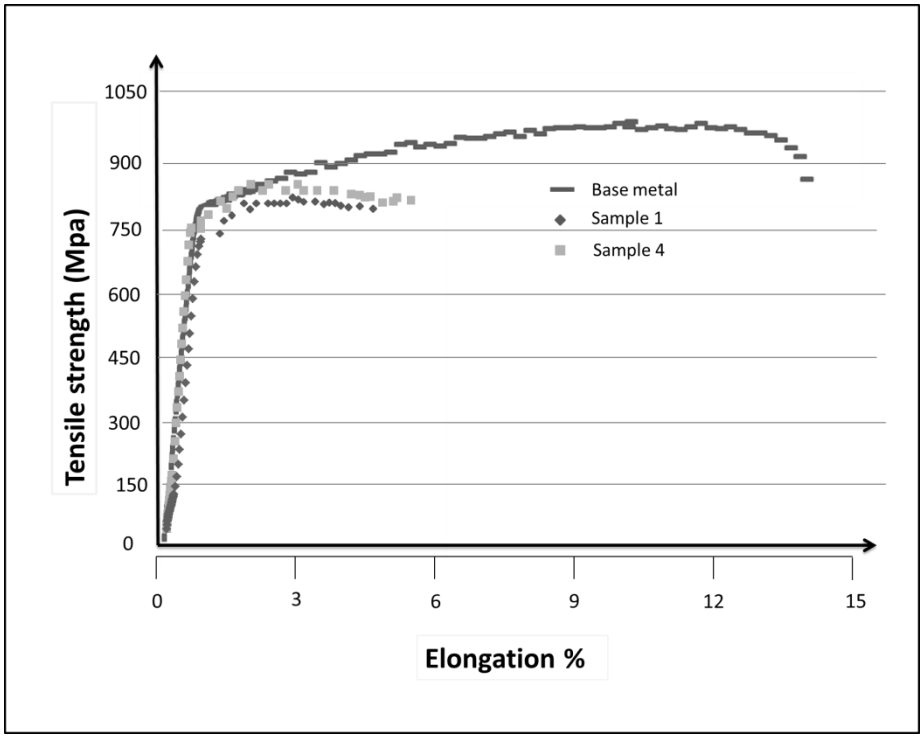

Fig. 10 Stress-strain curves for sample 1

3.5 Fracture surface analysis

The fracture of the welds occurred in the first part of the plastic field. As described in the paragraph 3.4, brittle structures formed during the solidification of the weld pool. Although the weld pool protection against contamination by atmospheric gases, a certain amount of brittle phases, such as oxides and nitrides, formed. Martensitic structures, formed because of the rapid cooling rate. Figure 11shows the fracture surfaces of parent metal specimen.

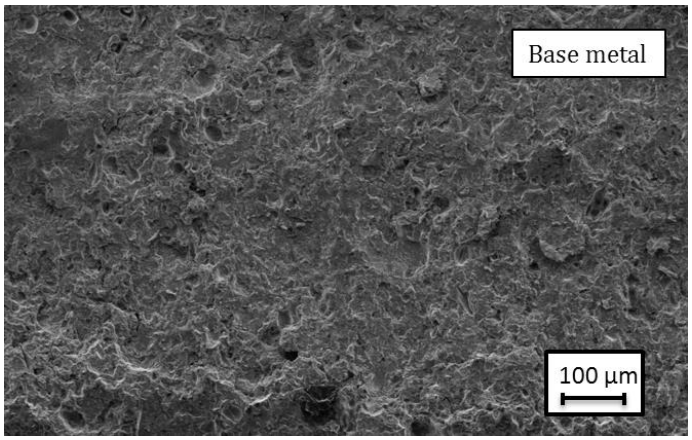

Fig. 11 Fracture surface of parent metal sample

The fracture surface of the parent metal was found to be quite uniform with rounded edges. The crack propagation growth direction seemed to be mostly perpendicular to the axis of the specimen. Figures 12 and 13 show the fracture surfaces of sample 4 and 1, respectively. As discussed in the paragraphs 3.1 and 3.2 the thermal process altered the homogeneity of the parent metal. Microstructure, chemical composition, distribution of phases and alloying elements varied leading to the alteration of mechanical properties. Liu et al. demonstrated that the microstructure gradient in the FZ of laser welded Ti alloy plates promotes crack initiation and fatigue damage [25]. Since during the welding local hardening and deformations occur because of spatially variable thermal cycles, the properties result to be not uniform in space. Probably, also a certain amount of micro-segregations formed. They derived from the accumulation of rejected solute and impurity between growing crystals. These also favored non-uniform hardening and embrittlement.

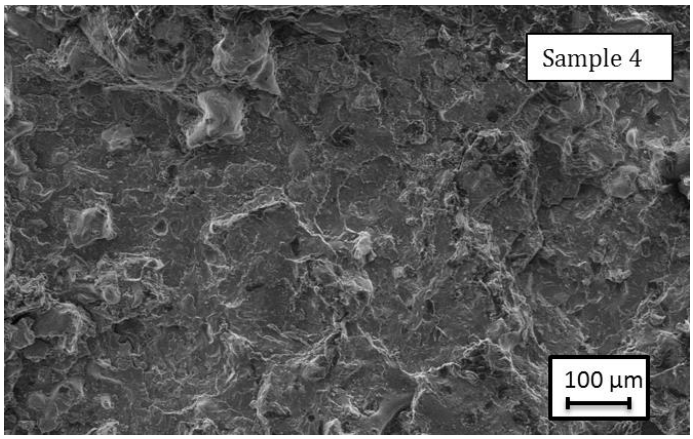

Fig. 12 Fracture surface of sample 4.

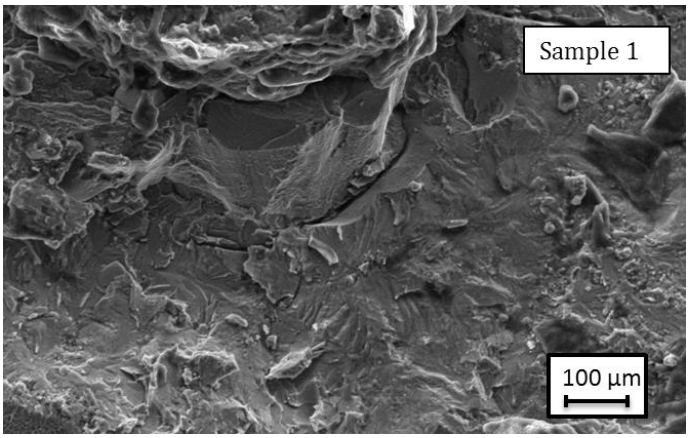

Fig. 13 Fracture surface of sample 1.

Since failures of samples 1 and 4 occurred in the FZ at the beginning of the plastic field, the surfaces appeared non-homogeneous, with sharped edges. β grains and randomly oriented martensite deflected the crack path, leading to local cleavage fracture. In particular, sample 4 (fig. 12) exhibited a slight higher ductility. Fine striations indicated localized plastic deformations, which led to a slight increase in toughness. Schneider et al. examined the fracture surfaces of laser welded α-β Ti alloy joints and detected a mixed mode brittle and ductile fracture [15].

On the other hand, sample 1 (fig. 13) exhibited several flat surface zones, probably surrounding the origin of cracks. Thus, the surface fracture of the parent metal exhibited ductile fracture morphology, while samples 1 and 4 indicated a brittle fracture mode in a large part of the surface.

4. Conclusions

This paper has served to characterize in detail the experimental results of Yb fiber CW laser welding of Ti6Al4V alloy in butt configuration. The main features of full penetration welds were studied. The following results were obtained.

- The linear energy expressed the heat input provided to the weld samples. It resulted a highly influencing parameter for the bead shape. High linear energy promoted an X-shaped bead, whereas low one promoted the formation of a V-shaped bead.
- The analysis of the micro-structural properties confirmed the formation of hard and brittle martensite structures in the FZ.
- The weld pool was efficiently shielded by adopting a reliable system of gas supplying. Contaminations and oxidations were satisfactory prevented.
- The mean ultimate tensile strength exceeded the 80% of the tested parent metal. The hard and brittle phase reduced the elongation to 4-5%.

The results account for a good weldability of Ti6Al4V alloy using a fiber laser. The authors will tackle the concerns about the weld ductility in future work on the analysis of pre-heating cycles and thermo-mechanical treatment.

References

[1] Veiga C, Davim J P, Loureiro A J R. Properties and applications of titanium alloys: a brief review. ADV. Mater. Sci. 2012; 32:133-148.

[2] Vinicius A R Henriques. Titanium production for aerospace applications. Journal of Aerospace Technology and Management 2009; 1.

[3] Peters M, Kumpfert J, Ward C H, Leyens C. Titanium alloys for aerospace applications. Advanced Engineering Materials 2003; 5, No 6.

[4] Elias C N, Lima J H C, Valiev R, Meyers M A. Biomedical applications of titanium and its alloys. Biological materials science overview 2008.

[5] Saresh N, Gopalakrishna Pillai M, Mathew J. Investigation into the effects of electron beam welding on thick Ti-6Al-4V titanium alloy. Journal of materials processing technology 2007; 192-193: 83-88.

[6] Luthabai S, Jarvis B L, Barton K J. Comparison of keyhole and conventional gas tungsten arc welds in commercially pure titanium. Materials Science and Engineering 2001; 299: 81-93.

[7] Greenwell T, Ramulu M, Labossiere P. Characterization of tensile behavior in friction stir-welded titanium alloy, Ti-6Al-4V. Proceedings of the SEM Annual Conference; 2009.

[8] Mironov S, Sato Y S, Kokawa H. Development of grain structure during friction stir welding of pure titanium. ActaMaterialia 2009; 57: 4519– 4528.

[9] Balasubramanian M, Jayabalan V, Balasubramanian V. Effect of pulsed gas tungsten arc welding on corrosion behavior of Ti–6Al–4V titanium alloy. Materials and Design 2008; 29: 1359–1363.

[10] Li R, Li Z, ZhuaY, Ronga L. A comparative study of laser beam welding and laser–MIG hybrid welding of Ti–Al–Zr–Fe titanium alloy. Materials Science and Engineering 2011; 528: 1138–1142.

[11] Sánchez Amaya J M, Amaya-Vázquez M R, Botana F J. Laser welding of light metal alloys: aluminium and titanium alloys. Handbook of Laser Welding Technologies 2013: 215–254.

[14 bis] Costa A, Quintino L, Miranda R, Yapp. Analysis of beam material interaction in welding of Titanium with fiber lasers. Materials and Manufacturing Process, 2007, 22, 798-803.

[14] Caiazzo F, Alfieri V, Corrado G, Cardaropoli F, Sergi V. Investigation and optimization of laser welding of Ti-6Al-4 V titanium alloy plates. Journal of Manufacturing Science and Engineering, Transactions of the ASME 2013; 135 (6): 061012.

[15] Schneider A, Gumenyuk A, Lammers M, Malletschek A. Laser beam welding of thick titanium sheets in the field of marine technology. Physics Procedia 2014; 56: 582-590.

[16] Akman E, Demir A, Canel T, Sınmazcelik T. Laser welding of Ti6Al4V titanium alloys. Journal of materials processing technology 2009; 209: 3705–3713.

[17] Squillace A, prisco U, Ciliberto S, Astarita A. Effect of welding parameters on morphology and mechanical properties of Ti-6Al-4V laser beam welded butt joints. Journal of materials processing technology 2012 ;212: 427-436.

[18] Gao X-L, Zhang L-J, Liu J, J-X Zhang. Porosity and microstructure in pulsed Nd:YAG laser welded Ti6Al4V sheet. Journal of Materials Processing Technology 2014; 214:1316–1325.

[19] Casalino G, Curcio F, Memola Capece Minutolo F. Investigation on Ti6Al4V laser welding using statistical and Taguchi approaches. Journal of Materials Processing Technology 2005; 167: 422-428.

[21] Katayama S. Handbook of laser welding technologies. Woodhead Publishing Series in Electronic and Optical Materials, Elsevier Science & Technology, Uk, 2013.

[22] Daurelio G. Il Dau: un'unità di misura dell'efficienza di processo nel taglio, saldatura, microforatura e trattamenti termici superfciali a laser. Rivista italiana della saldatura 2011; No 5: 659-671.

[23] Ion J C. Laser processing of engineering materials: Principles, Procedures and Industrial Applications. Elsevier Butterworth-Heinrmann, UK, 2005.

[24] Zhang L J, Zhang J X, Gumenyuk A, Rethmeier M, Na S J. Numerical simulation of full penetration laser welding of thick steel plate with high power high brightness laser. Journal of materials processing technology 2014; 214: 1710-1720.

[25] Liu J, Gao X-L, Zhang L-J, Zhang J-X. A study of fatigue damage evolution on pulsed Nd:YAG Ti6Al4V laser welded joints. Engineering Fracture Mechanics 2014; 117: 84–93.